

Wind-Induced Changes to Surface Gravity Wave Shape in Shallow Water

Thomas Zdyrski¹†, and Falk Feddersen¹

¹ Scripps Institution of Oceanography, UCSD, La Jolla, CA 92092-0209, USA

(Received xx; revised xx; accepted xx)

Wave shape (*e.g.* wave skewness and asymmetry) impacts sediment transport, remote sensing and ship safety. Previous work showed that wind affects wave shape in intermediate and deep water. Here, we investigate the effect of wind on wave shape in shallow water through a wind-induced surface pressure for different wind speeds and directions. A multiple-scale analysis of long waves propagating over a shallow, flat bottom and forced by a Jeffreys-type surface pressure produces a Korteweg-de Vries (KdV)-Burgers equation for the wave profile. The evolution of a symmetric, solitary wave initial condition is calculated numerically. The resulting wave grows (decays) for onshore (offshore) wind and becomes asymmetric, with the rear face showing the largest shape changes. The wave profile's deviation from a reference solitary wave shows a bound, dispersive, decaying tail. The onshore wind increases the wave's energy and skewness with time while decreasing the wave's asymmetry, with the opposite holding for offshore wind. The corresponding wind speeds are shown to be physically realistic, and the shape changes are explained as slow growth followed by rapid evolution according to the unforced KdV equation.

1. Introduction

The study of wind and ocean wave interactions began with Jeffreys (1925) and continues to be an active field of research (*e.g.*, Janssen 1991; Donelan *et al.* 2006; Sullivan & McWilliams 2010). Many theoretical studies (*e.g.*, Jeffreys 1925; Miles 1957; Phillips 1957) focus on calculating wind-induced growth rates and often employ phase-averaging techniques. However, wind can also influence wave shape, quantified by third-order shape statistics such as skewness and asymmetry, corresponding to vertical and horizontal asymmetry, respectively (*e.g.*, Leykin *et al.* 1995; Feddersen & Veron 2005; Zdyrski & Feddersen 2020). Wave shape influences sediment transport and modulates beach morphodynamics (*e.g.*, Drake & Calantoni 2001; Hoefel & Elgar 2003), while wave skewness affects radar altimetry signals (*e.g.*, Hayne 1980) and asymmetry modulates ship responses to wave impacts (*e.g.*, Soares *et al.* 2008).

Waves in shallow water, where $kh \ll 1$ (with h the water depth and $k = 2\pi/\lambda$ the wavenumber), differ qualitatively from those in intermediate to deep water where $kh \sim 1$ or $\gg 1$, respectively. For waves with small amplitudes $a_0 \ll h$, leveraging the small parameters $a_0/h \sim (kh)^2 \ll 1$ yields the Boussinesq equations with weak dispersion and nonlinearity. A special class of waves formed when dispersion balances nonlinear focusing are known as solitary waves and appear in environments ranging from nonlinear optical pulses (*e.g.*, Kivshar 1993) to astrophysical dusty plasmas (*e.g.*, Sahu & Tribeche 2012). One of the simplest equations displaying solitary waves is the Korteweg-de Vries (KdV) equation, which incorporates dispersion and nonlinearity. When augmented with a dissipative term, this becomes the KdV-Burgers equation, with applications to damped internal tides (*e.g.*, Sandstrom & Oakey 1995), electron waves

† Email address for correspondence: tzdyrski@ucsd.edu

in graphene (*e.g.*, Zdyrski & McGreevy 2019) and viscous flow in blood vessels (*e.g.*, Antar & Demiray 1999). To investigate wind and surface wave interactions in shallow water, we introduce a wind-induced pressure term to the Boussinesq equations in section 2. The resulting KdV-Burgers equation governs a solitary wave’s evolution, which we solve numerically to yield the wave energy, skewness and asymmetry in section 3. We calculate the wind speed, discuss the asymmetry and compare our results to intermediate- and deep-water waves in section 4.

2. Derivation of the KdV-Burgers equation

2.1. Governing equations

We treat the flow as irrotational and inviscid and neglect surface tension by considering length scales much greater than 2 cm. Furthermore, we restrict to planar wave propagation in the $+x$ direction. Finally, we choose a coordinate system with $z = 0$ at the mean water level and a horizontal, flat bottom located at $z = -h$. Then, the incompressibility condition and standard boundary conditions are

$$0 = \phi_{xx} + \phi_{zz} \quad \text{on} \quad -h < z < \eta, \quad (2.1)$$

$$0 = \phi_z \quad \text{on} \quad z = -h, \quad (2.2)$$

$$\phi_z = \eta_t + \phi_x \eta_x \quad \text{on} \quad z = \eta, \quad (2.3)$$

$$0 = \frac{p}{\rho_w} + g\eta + \phi_t + \frac{1}{2}[\phi_x^2 + \phi_z^2] \quad \text{on} \quad z = \eta. \quad (2.4)$$

Here, $\eta(x, t)$ is the wave profile, $\phi(x, z, t)$ is the flow’s velocity potential related to the velocity $\mathbf{u} = \nabla\phi$, $p(x, t)$ is the surface pressure, g is the gravitational acceleration and ρ_w is the water density. We used ϕ ’s gauge freedom to absorb the Bernoulli ‘constant’ $C(t)$ in the dynamic boundary condition. We are seeking a solitary, progressive wave which decays at infinity, $\eta(\mathbf{x}, t) \rightarrow 0$ as $|\mathbf{x}| \rightarrow \infty$, with similar conditions on \mathbf{u} . We choose a coordinate system where the average bottom horizontal velocity vanishes,

$$\overline{\frac{\partial\phi}{\partial x}} = 0 \quad \text{on} \quad z = -h, \quad (2.5)$$

with the overline a spatial average $\overline{f} := \lim_{L \rightarrow \infty} \int_{-L}^L f dx / (2L)$. Additionally, we assume the surface pressure $p(x, t)$ is a Jeffreys-type forcing (Jeffreys 1925),

$$p(x, t) = P \frac{\partial\eta(x, t)}{\partial x}. \quad (2.6)$$

Here, P is proportional to $(U - c)^2$, with c the phase speed and U the wind speed (*cf.* section 4.1), and $P > 0$ corresponds to (‘onshore’) wind in the same direction as the wave while $P < 0$ denotes (‘offshore’) wind opposite the wave. We use a Jeffreys forcing for its analytic simplicity and clear demonstration of wind-wave coupling. Jeffrey’s separated sheltering mechanism is likely only relevant in special situations (*e.g.* near breaking, Banner & Melville 1976, or for steep waves under strong winds, Tian & Choi 2013; Touboul & Kharif 2006). Additionally, numerical simulations of sinusoidal waves suggest the peak surface pressure is shifted approximately 135° from the wave peak, while Jeffreys would give a 90° shift (Husain *et al.* 2019). However, a fully dynamic coupling between wind and waves—necessary for an accurate surface pressure over a non-sinusoidal, dynamic water surface—is outside the scope of this paper.

2.2. Non-dimensionalization

We non-dimensionalize our system with the known characteristic scales: the horizontal length scale L over which η changes rapidly, expressed as an effective wavenumber $k_E :=$

$2\pi/L$; the (initial) wave amplitude $a_0 = H_0/2$ (*i.e.* half the wave height H_0); the depth h ; the gravitational acceleration g ; and the wind speed U , expressed as a pressure magnitude $P \propto \rho_a(U - c)^2$. Denoting non-dimensional variables with primes, we have

$$\begin{aligned} x &= \frac{x'}{k_E} = h \frac{x'}{\sqrt{\mu_E}}, & t &= \frac{t'}{k_E \sqrt{gh}} = \frac{t'}{\sqrt{\mu_E}} \sqrt{\frac{h}{g}}, & \eta &= a_0 \eta' = h \varepsilon \eta', \\ z &= h z', & P &= \varepsilon P' \frac{\rho_w g}{k_E} = \frac{\varepsilon}{\sqrt{\mu_E}} P' \rho_w g h, & \phi &= \phi' \frac{a_0}{k_E} \sqrt{\frac{g}{h}} = \frac{\phi' \varepsilon}{\sqrt{\mu_E}} \sqrt{gh^3}. \end{aligned} \quad (2.7)$$

Our system's dynamics are controlled by three small, non-dimensional parameters: $\varepsilon := a_0/h$, $\mu_E := (k_E h)^2$ and $P k_E / (\rho_w g)$. We will later require $\mathcal{O}(\varepsilon) = \mathcal{O}(\mu_E) = \mathcal{O}(P k_E / (\rho_w g))$. Now, our non-dimensional equations take the form

$$0 = \mu_E \phi'_{x'x'} + \phi'_{z'z'} \quad \text{on} \quad -1 < z' < \varepsilon \eta', \quad (2.8)$$

$$0 = \phi'_{z'} \quad \text{on} \quad z' = -1, \quad (2.9)$$

$$\phi'_{z'} = \mu_E \eta'_{t'} + \varepsilon \mu_E \phi'_{x'} \eta'_{x'} \quad \text{on} \quad z' = \varepsilon \eta', \quad (2.10)$$

$$0 = \varepsilon P' \eta'_{x'} + \eta' + \phi'_{t'} + \frac{1}{2} \left(\varepsilon \phi'_{x'}{}^2 + \frac{\varepsilon}{\mu_E} \phi'_{z'}{}^2 \right) \quad \text{on} \quad z' = \varepsilon \eta'. \quad (2.11)$$

We will drop the primes throughout the remainder of this section for readability.

2.3. Boussinesq equations, multiple-scale expansion, KdV equation, and initial condition

Here, we modify the Boussinesq equation's derivation provided by Mei *et al.* (2005) by including the surface pressure forcing in (2.4). First we Taylor expand the velocity potential ϕ about the bottom, $z = -1$,

$$\phi(x, y, z, t) = \sum_{n=0}^{\infty} (z+1)^n \phi_n(x, y, t). \quad (2.12)$$

Then, a standard calculation (*e.g.*, Mei *et al.* 2005) using Laplace's equation (2.8) and the bottom boundary condition (2.9) yields an expansion of ϕ in terms of $\mu_E \ll 1$,

$$\phi = \phi_0 - \frac{1}{2} \mu_E (z+1)^2 \partial_x^2 \phi_0 + \frac{\mu_E^2}{24} (z+1)^4 \partial_x^4 \phi_0 + \mathcal{O}(\mu_E^3). \quad (2.13)$$

For convenience, we define $\varphi := \phi_0$. Substituting this expansion into the two remaining boundary equations, (2.10) and (2.11), and recalling that they are evaluated at $z = \varepsilon \eta$, we have reduced our system to the Boussinesq equations with a pressure forcing term,

$$\partial_t \eta + \partial_x^2 \varphi + \varepsilon \partial_x (\eta \partial_x \varphi) - \frac{1}{6} \mu_E \partial_x^4 \varphi = \mathcal{O}(\mu_E^2), \quad (2.14)$$

$$\partial_t \varphi + \varepsilon P \partial_x \eta + \eta - \frac{1}{2} \mu_E \partial_t \partial_x^2 \varphi + \frac{1}{2} \varepsilon (\partial_x \varphi)^2 = \mathcal{O}(\mu_E^2). \quad (2.15)$$

Further, we will now assume $\mathcal{O}(\varepsilon) = \mathcal{O}(\mu_E) \ll 1$.

We now expand t using multiple time scales $t_n = \varepsilon^n t$ for $n = 0, 1$, so all time derivatives become $\partial_t \rightarrow \partial_{t_0} + \varepsilon \partial_{t_1}$. Then, we write η and φ in asymptotic series of ε ,

$$\eta(x, t) = \sum_{k=0}^{\infty} \varepsilon^k \eta_{k+1}(x, t_0, t_1) \quad \text{and} \quad \varphi(x, t) = \sum_{k=0}^{\infty} \varepsilon^k \varphi_{k+1}(x, t_0, t_1). \quad (2.16)$$

Now, we will reduce the Boussinesq equations, (2.14) and (2.15), to the KdV equation following a similar method to Mei *et al.* (2005). Collecting order-one terms $\mathcal{O}(\varepsilon^0)$ from

(2.14) and (2.15) gives

$$\frac{\partial \eta_0}{\partial t_0} + \frac{\partial^2 \varphi_0}{\partial x^2} = 0 \quad \text{and} \quad \eta_0 + \frac{\partial \varphi_0}{\partial t_0} = 0, \quad (2.17)$$

yielding left- and right-moving waves. Restricting to right-moving waves gives

$$\varphi_0 = f_0(x - t_0, t_1) \quad \text{and} \quad \eta_0 = f'_0(x - t_0, 1) \quad \text{with} \quad f'_0 := \left. \frac{\partial f_0(\theta, t_1)}{\partial \theta} \right|_{\theta=x-t_0}. \quad (2.18)$$

Continuing to the next order of perturbation theory, we retain terms of order $\mathcal{O}(\varepsilon)$,

$$\frac{\partial \eta_1}{\partial t_0} + \frac{\partial^2 \varphi_1}{\partial x^2} = -\frac{\partial \eta_0}{\partial t_1} - \frac{\partial}{\partial x} \left(\eta_0 \frac{\partial \varphi_0}{\partial x} \right) + \frac{1}{6} \frac{\mu_E}{\varepsilon} \frac{\partial^4 \varphi_0}{\partial x^4}, \quad (2.19)$$

$$\eta_1 + \frac{\partial \varphi_1}{\partial t_0} = -P \frac{\partial \eta_0}{\partial x} - \frac{\partial \varphi_0}{\partial t_1} + \frac{1}{2} \frac{\mu_E}{\varepsilon} \frac{\partial^3 \varphi_0}{\partial t_0 \partial^2 x} - \frac{1}{2} \left(\frac{\partial \varphi_0}{\partial x} \right)^2. \quad (2.20)$$

Inserting our leading order solutions for η_0 and φ_0 while eliminating η_1 gives

$$\left(\frac{\partial^2}{\partial x^2} - \frac{\partial^2}{\partial t_0^2} \right) \varphi_1 = -2 \frac{\partial f'_0}{\partial t_1} + P \frac{\partial^2 \eta_0}{\partial t_0 \partial x} - 3 f'_0 f''_0 - \frac{1}{3} \frac{\mu_E}{\varepsilon} f_0^{(4)}. \quad (2.21)$$

The homogeneous equation is again the shallow-water wave equation for φ_1 . Since the right-hand side is a resonant forcing, it must vanish. Thus, converting back to η_0 gives the Korteweg-de Vries (KdV)-Burgers equation,

$$\frac{\partial \eta_0}{\partial t_1} + \frac{3}{2} \eta_0 \frac{\partial \eta_0}{\partial x} + \frac{1}{6} \frac{\mu_E}{\varepsilon} \frac{\partial^3 \eta_0}{\partial x^3} = -P \frac{1}{2} \frac{\partial^2 \eta_0}{\partial x^2}. \quad (2.22)$$

The pressure term, $P \partial_x^2 \eta_0$, acts as a positive viscosity for offshore, damping wind or a negative viscosity when onshore wind causes wave growth. Note that (2.22) has a rescaling symmetry, with $\mu_E \rightarrow \lambda^2 \mu_E$ equivalent to taking $(x, t_0, t_1, P) \rightarrow (x, t_0, t_1, P)/\lambda$. Therefore, we fix the length scale (equivalently, k_E) by choosing $\mu_E = 6\varepsilon$.

The solitary wave solutions of the unforced ($P = 0$) KdV equation balance dispersion $\partial_x^3 \eta_0$ with focusing nonlinearity $\eta_0 \partial_x \eta_0$ and have the form (*e.g.*, Mei *et al.* 2005)

$$\eta_0 = H_0 \operatorname{sech}^2 \left(\frac{x}{\Delta} \right) \quad \text{with} \quad \Delta = \sqrt{\frac{8}{H_0}}, \quad (2.23)$$

in a co-moving frame with $H_0 > 0$ an order-1 parameter. We use (2.23) for our initial condition and choose $H_0 = 2$ so the initial, dimensional amplitude a_0 is half the wave height (*cf.* section 2.2). The dissipative term $P \partial_x^2 \eta_0$ in (2.22) disrupts the solitary wave's balance of dispersion and nonlinearity, inducing shape changes and growth/decay. The KdV-Burgers equation has no known, solitary wave solutions, so we will solve it numerically.

2.4. Numerics and shape statistics

To solve (2.22) numerically, we will use a spatial domain with periodic boundary conditions and $N_x = 1600$ points spread over a domain of length $L = 80$. This yields a spacing $\Delta x = 0.05$, with $x = -L/2, -L/2 + \Delta x, \dots, L/2 - \Delta x$. The simulation runs from $t_1 = 0$ to $t_1 = T = 3$, inclusive, with $N_t = 4.8 \times 10^5$ points, yielding a spacing $\Delta t_1 = T/(N_t - 1) \approx 6.25 \times 10^{-6}$. We found that linearly ramping up P from 0 at $t_1 = 0$ to its full value at $t_1 = \varepsilon$, or full, dimensional time $t = \sqrt{g h} k_E$ (*i.e.* the time required to cross the effective wavelength $2\pi/k_E$, or 'wave-crossing time') did not qualitatively modify the results, so we do not utilize such a ramp-up here.

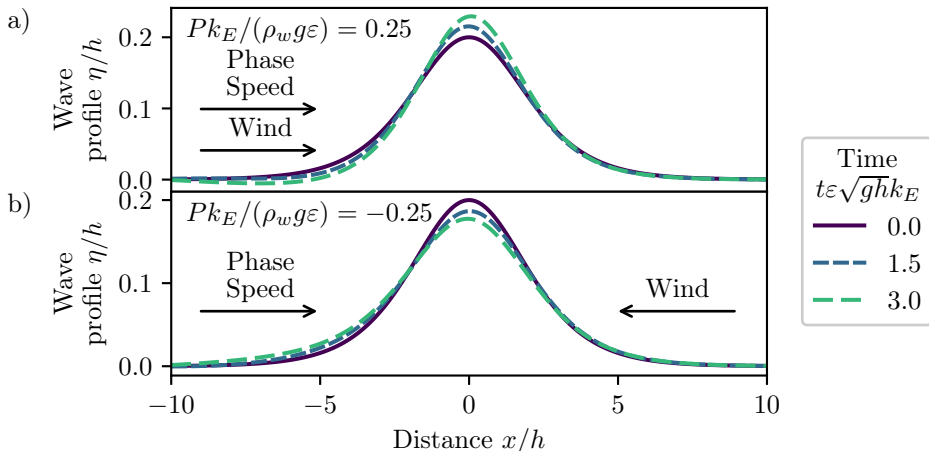


Figure 1. Solitary wave evolution under (a) onshore and (b) offshore wind-induced surface pressure in the frame of the unforced solitary wave. Non-dimensional wave height η/h versus non-dimensional distance x/h for $\varepsilon = 0.1$, $\mu_E = 0.6$, $|Pk_E/(\rho_w g \varepsilon)| = 0.25$, and non-dimensional slow times $t'_1 = t\varepsilon\sqrt{gh}k_E = 0, 1.5$ and 3, as indicated in the legend. Only a subset of the full spatial domain is shown. The arrows denote the wave propagation (phase speed) and wind direction.

We discretize (2.22) in space using a second-order central finite difference method and in time using a third-order Runge-Kutta scheme. For numerical stability, we must also include a hyperviscosity term, $-\nu_{\text{bi}}\partial_x^4\eta_0$ with $\nu_{\text{bi}} = 3 \times 10^{-3}$, on the right-hand side of (2.22). This hyperviscosity has minimal effect on the wave evolution as the normalized root-mean-square difference between the unforced ($P = 0$) profile η at $t'_1 = 3$ and the initial condition η_0 is $\sqrt{\langle(\eta - \eta_0)^2\rangle/\langle\eta_0^2\rangle} = 2 \times 10^{-3}$. We quantify the wave shape with the wave energy E , skewness Sk and asymmetry As ,

$$E := \langle\eta^2\rangle, \quad \text{Sk} := \frac{\langle\eta^3\rangle}{\langle\eta^2\rangle^{3/2}} \quad \text{and} \quad \text{As} := \frac{\langle\mathcal{H}\{\eta^3\}\rangle}{\langle\eta^2\rangle^{3/2}}, \quad \text{with} \quad \langle f \rangle := \frac{1}{L} \int_{-L/2}^{L/2} f \, dx. \quad (2.24)$$

Here, \mathcal{H} is the Hilbert transform. Since these definitions depend on the domain size L , we normalize the energy E and skewness Sk by their initial values.

3. Results

We study the pressure magnitude's effect on solitary wave evolution and shape by varying the KdV-Burgers equation's (2.22) one free parameter, $Pk_E/(\rho_w g \varepsilon)$, with emphasis on the contrast between onshore ($P > 0$) and offshore wind ($P < 0$). We revert to denoting non-dimensional variables with primes and dimensional ones without.

The wave profile η/h snapshots in fig. 1 qualitatively show how the wave shape evolves over non-dimensional slow time $t'_1 = t\varepsilon\sqrt{gh}k_E$ in the unforced solitary wave's frame. The onshore wind generates wave growth, apparent at the wave crest $x = 0$ (fig. 1(a)), whereas the onshore wind causes decay (fig. 1(b)). The wind also slightly changes the phase speed, with the wave's acceleration (deceleration) under an onshore (onshore) wind visible by the slight advancing (receding) of the crest. This is expected due to the dependence of (unforced) solitary waves' phase speed $c = H/2$ on the growing/decaying wave height (*e.g.*, Mei *et al.* 2005). Additionally, despite the wave starting from a symmetric, solitary-wave initial condition, the wind induces a horizontal asymmetry in the wave shape, particularly on the rear face ($x < 0$) of the wave. The offshore wind (fig. 1(b)) raises the rear base of the wave (near $x/h = -6$) relative to its initial profile (purple line), but the onshore

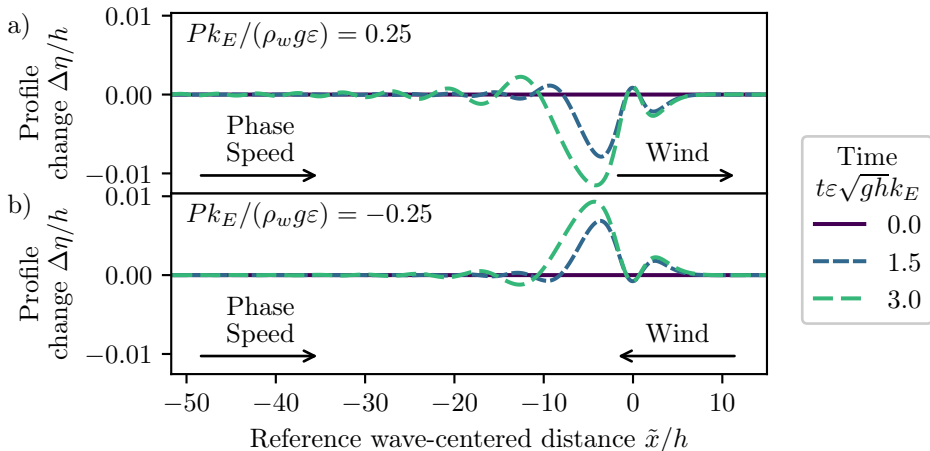


Figure 2. The non-dimensional profile change $\Delta\eta/h$ between the surface profile and reference solitary wave (2.23) under (a) onshore and (b) offshore Jeffreys forcing versus non-dimensional reference wave-centered distance \tilde{x}/h . Results are shown for $\varepsilon = 0.1$, $\mu_E = 0.6$, $|Pk_E/(\rho_w g \varepsilon)| = 0.25$, and non-dimensional slow times $t'_1 = t\varepsilon\sqrt{g\tilde{h}k_E} = 0, 1.5$ and 3, as indicated in the legend. Only a subset of the full spatial domain is shown. The arrows denote the direction of wave propagation (phase speed) or wind direction.

wind (fig. 1(a)) depresses the rear face and forms a small depression below the still water level at $t\varepsilon\sqrt{g\tilde{h}k_E} = 3$ (green line). Finally, the onshore wind (fig. 1(a)) increases the maximum wave-slope magnitude with time while the offshore wind (fig. 1(b)) decreases it, though the windward side of the wave becomes steeper than the leeward side for both winds (up to 8% steeper for the time period shown).

To further examine the wind-induced wave asymmetry, we fit η to a reference solitary wave profile η_{ref} (2.23) by minimizing the L_1 difference, yielding the reference height $H_{\text{ref}}(t_1)$ and peak location $x_{\text{ref}}(t_1)$. The profile change is defined as $\Delta\eta(x) := \eta - \eta_{\text{ref}}$ and is shown as a function of the reference wave-centered distance $\tilde{x} := x - x_{\text{ref}}$ in fig. 2. Notice that the profile change begins near the front face of the wave and has extrema for negative \tilde{x} but with opposite signs for onshore and offshore winds. Additionally, the magnitude of the extrema decay quickly with distance in the $-\tilde{x}$ direction. Finally, note that the onshore (offshore) wind generates a small peak (trough) at $\tilde{x} = 0$ and two small troughs (peaks) near $\tilde{x}/h = \pm 3$, with the $\tilde{x} < 0$ extrema larger than the $\tilde{x} > 0$ one.

The effect of wind on wave shape is quantified by the time evolution of wave shape statistics—energy, skewness and asymmetry—for onshore and offshore wind (fig. 3). We plot all cases for initial steepness $\varepsilon = 0.1$ up to slow time $t\varepsilon\sqrt{g\tilde{h}k_E} = 3$, corresponding to $3/\varepsilon = 30$ wave-crossing times, $\sqrt{g\tilde{h}k_E}$. The unforced case ($P = 0$) displays constant shape statistics and zero asymmetry, as expected. The normalized energy E/E_0 shows different growth/decay rates: the onshore wind ($P > 0$) causes accelerating wave growth while the offshore wind ($P < 0$) causes slowing wave decay (fig. 3(a)). The onshore (offshore) wind causes the wave to become more (less) skewed over time, with the normalized skewness nearly symmetric about unity with respect to $\pm P$. Finally, the onshore wind causes a backwards tilt and negative asymmetry while the offshore wind increases the asymmetry and causes a forward tilt, which was also seen in fig. 1. Notice that $|As|$ is larger for onshore winds than offshore winds. Since the definitions of the skewness and asymmetry are insensitive to waveform scaling $\eta \rightarrow \lambda\eta$, this effect is not simply caused by the wave's growth/decay. Instead, the onshore wind generates a larger dispersive tail (fig. 2), which is the asymmetric wave component.

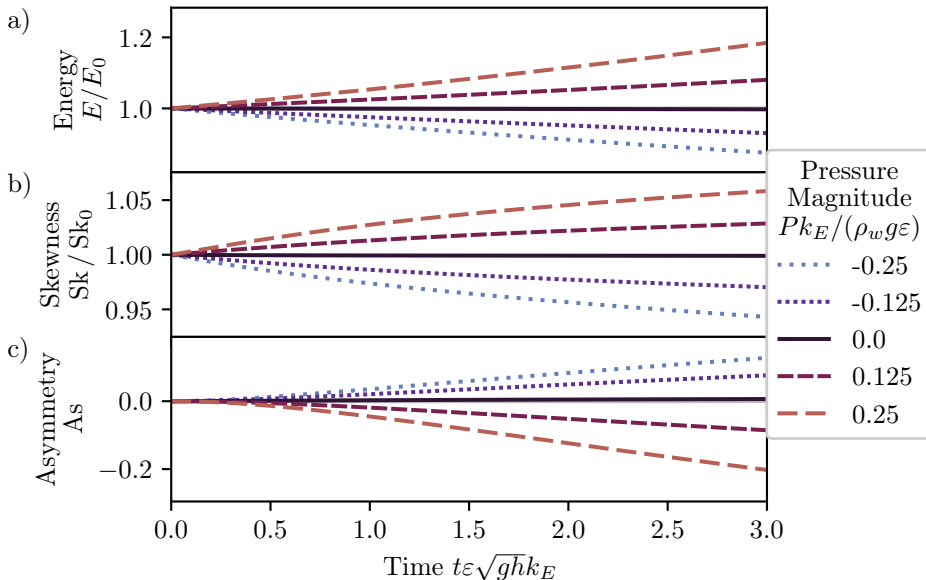


Figure 3. Solitary wave shape statistics under onshore and offshore Jeffreys forcing versus non-dimensional slow time $t'_1 = t\varepsilon\sqrt{gh}k_E = 0$ to 3. The (a) energy (normalized by the initial energy), (b) skewness (normalized by the initial skewness) and (c) asymmetry are defined in (2.24). Results are shown for $\varepsilon = 0.1$, $\mu_E = 0.6$ and pressure magnitude $Pk_E/(\rho_w g \varepsilon)$ up to 0.25, as indicated in the legend. The solid black line is the unforced case, $P = 0$, and shows no growth or asymmetry and a constant skewness.

4. Discussion

4.1. Wind speed estimation

We now relate the non-dimensional pressure magnitude $Pk_E/(\rho_w g) = \mathcal{O}(\varepsilon)$ to the wind speed. First, we need a relationship between the surface pressure and wave energy E (2.24), which we can approximate using the standard procedure (*e.g.*, Mei *et al.* 2005) of multiplying the (non-dimensional, denoted by primes) KdV-Burgers equation (2.22) by η'_0 and integrating from $x' = -\infty$ to ∞ to obtain

$$\frac{\partial}{\partial t'_1} \int_{-\infty}^{\infty} \eta'^2_0 dx' = \int_{-\infty}^{\infty} P' \left(\frac{\partial \eta'_0}{\partial x'} \right)^2 dx'. \quad (4.1)$$

The left integral is the non-dimensional energy (2.24), so re-dimensionalizing and converting back to the full time t gives the energy growth rate γ ,

$$\frac{\gamma}{ck_E} := \frac{1}{ck_E E} \frac{\partial E}{\partial t} = \frac{Pk_E}{\rho_w g} \frac{\langle (\partial_x \eta)^2 \rangle}{\langle (k_E \eta)^2 \rangle} = \frac{1}{5} \frac{Pk_E}{\rho_w g}, \quad (4.2)$$

with $c = \sqrt{gh}$ the phase speed and the angle brackets evaluated with the initial, solitary wave profile (2.23). Alternatively, we can numerically fit the energy growth rate to

$$E \propto \frac{1}{(1 - \gamma t)^2} \quad \text{with} \quad \gamma := b \left[\frac{Pk_E}{\rho_w g} \right] ck_E, \quad (4.3)$$

resulting in $b = 0.10000 \pm 0.00009$. Equation (4.3) has the same functional form and similar growth rate $\gamma = (2/15)(Pk_E/\rho_w g \varepsilon)ck$ to that derived for solitary waves using a secondary multiple-scale approximation of the KdV-Burgers equation (Zdyrski & McGreevy 2019). Note that the exponential energy growth (4.2) correctly approximates the rational

energy growth (4.3) for small times $\gamma t \ll 1$, and both expressions are consistent with the observed accelerating (decelerating) energy change for $P > 0$ ($P < 0$) in fig. 3.

Next, Jeffreys's (1925) theory relates the growth rate of periodic waves to the wind speed $U_{\lambda/2}$, measured at a height equal to half the wavelength $z = \lambda/2$, as

$$\frac{\gamma}{ck} = S_{\lambda/2} \frac{\rho_a}{\rho_w} \left(\frac{U_{\lambda/2}}{c} - 1 \right) \left| \frac{U_{\lambda/2}}{c} - 1 \right|, \quad (4.4)$$

with $S_{\lambda/2}$ a small, non-dimensional sheltering parameter potentially dependent on ε , μ_E and $U_{\lambda/2}/c$. Combining this with (4.2) gives

$$U_{\lambda/2} = c \left(1 \pm \sqrt{\frac{1}{5} \left| \frac{Pk_E}{\rho_w g} \right| \frac{\rho_w}{\rho_a} \frac{1}{S_{\lambda/2}}} \right). \quad (4.5)$$

Here, the \pm corresponds to onshore (+) or offshore (−) winds. Note that changing the wind direction (*i.e.* \pm sign) while holding the surface pressure magnitude $|Pk_E/(\rho_w g)|$ constant means onshore wind speeds $|U_{\lambda/2}|$ will be larger than offshore wind speeds.

We can evaluate (4.5) for the parameters of section 3: $\varepsilon = 0.1$, $\mu_E = 0.6$ and $Pk/(\rho_w g \varepsilon) = 0.25$. Donelan *et al.* (2006) parameterized $S_{\lambda/2}$ for periodic shallow-water waves with a dependence on airflow separation: $S_{\lambda/2} = 4.91 \varepsilon \sqrt{\mu}$ for our non-separated flow (according to their criterion), with $\mu := (kh)^2$. Assuming this holds approximately for solitary waves, we choose $\lambda = 2\pi/k_E = 20$ m to calculate the wind speed at $z = \lambda/2 = 10$ m. This choice corresponds to a depth of $h = 2.5$ m and initial wave height $H_0 = 0.5$ m and yields a wind speed of $U_{10} = 21$ m s^{−1}, a physically realistic wind speed for strongly forced shallow-water waves. Weaker wind speeds will induce smaller surface pressures and thus take longer to change the wave shape.

4.2. Physical mechanism of asymmetry generation

Our initial, symmetric solitary waves (2.23) are permanent-form solutions of the unforced KdV equation, so the pressure forcing term in the KdV-Burgers equation is responsible for the wave growth/decay and resultant shape changes and asymmetry, though not directly. Indeed, when the surface profile η is symmetric, the pressure forcing term $P\partial_x^2\eta$ preserves the initial symmetry. Instead, the pressure forcing causes a (symmetric) bound wave after a short time $\Delta t'_1 \ll 1$, which can be seen by considering the non-dimensional KdV-Burgers equation (2.22) in the unforced solitary wave's frame (fig. 1) at the initial time,

$$\left. \frac{\partial \eta'_0}{\partial t'_1} \right|_{t'_1=0} = -P' \frac{\partial^2}{\partial x'^2} \left[\operatorname{sech}^2 \left(\frac{x'}{2} \right) \right] \quad (4.6)$$

$$\implies \eta'_0(x', \Delta t'_1) = (2 - P' \Delta t'_1) \operatorname{sech}^2 \left(\frac{x'}{2} \right) + P' \Delta t'_1 \frac{3}{2} \operatorname{sech}^4 \left(\frac{x'}{2} \right). \quad (4.7)$$

The $P' \Delta t'_1$ terms generate a small peak (trough) at $x' = 0$ and small troughs (peaks) symmetrically in front and behind the wave peak for onshore (offshore) wind, which are apparent near $\tilde{x}/h \approx \pm 3$ in fig. 2. The small numerical value $|P'| = 0.25 \ll 1$ used in section 3 allows us to consider the wave's evolution as two steps with time scale separation. First, the pressure modifies the wave (4.7) on the slow time scale, and then the wave evolves on a fast time scale from this new profile according to unforced KdV evolution. This evolution is described by the inverse scattering transform, which shows that any localized, initial profile differing from (2.23) will split into discrete solitary waves and a bound, dispersive tail that decays behind ($x < 0$) the wave (*e.g.*, Mei *et al.* 2005). Prior

studies on shallow-water, KdV solitary waves have also noted this ubiquitous dispersive tail, such as figs. 8(b) and (c) of Hammack & Segur (1974). Hence, the symmetric disturbance induced by the pressure forcing (4.7) has two effects on the wave. First, the wind slowly changes the height and width of the initial solitary wave, which is reflected in the growth (decay) and narrowing (widening) under onshore (offshore) winds in fig. 1. Second, it quickly generates an asymmetric, dispersive tail behind the wave (fig. 2), producing a greater shape change on the wave's rear face (fig. 1). Finally, the different wind directions (*i.e.* pressure forcing signs) change the sign of the bound, dispersive tail and, hence, the sign of the asymmetry in fig. 3.

4.3. Comparison to intermediate and deep water

Zdyrski & Feddersen (2020) investigated the effect of wind on Stokes-like waves in intermediate to deep water. This study, with wind coupled to waves in shallow water, finds qualitative agreement with those intermediate- and deep-water results. The shallow-water asymmetry magnitude increases as the pressure magnitude P increases (fig. 3), and fig. 4(a) of Zdyrski & Feddersen (2020) displayed a similar trend for the corresponding Jeffreys pressure profile, with positive (negative) pressure increasing (decreasing) the asymmetry. Although Zdyrski & Feddersen (2020) compared their theoretical predictions to limited experimental results with $kh > 1$, there are no appropriate experiments on wind-induced changes to wave shape in shallow water for comparison with our results. In addition to the Jeffreys pressure profile employed here, Zdyrski & Feddersen (2020) also utilized a generalized Miles profile, only applicable to periodic waves, wherein the pressure was proportional to η shifted by a distance parameter ψ_P/k . Though this analysis focuses on solitary waves, we also investigated the effect of wind on periodic waves using the cnoidal-wave KdV solutions as initial conditions. However, these were omitted for brevity.

5. Conclusion

Prior results (Zdyrski & Feddersen 2020) in intermediate and deep water demonstrated that wind, acting through a wave-dependent surface pressure, can generate shape changes that become more pronounced in shallow water. Here, we utilized a multiple-scale analysis to couple weak wind with small, shallow-water waves, *i.e.* $a_0/h \sim (k_E h)^2 \sim Pk/(\rho_w g) \ll 1$. This gave a KdV-Burgers equation governing the wave profile η which was solved numerically with a symmetric, solitary wave initial condition. The deviations between the numerical results and a reference solitary wave had the form of a bound, dispersive tail, with differing signs for onshore and offshore wind. The tail's presence and shape are the result of a symmetric, pressure-induced shape change evolving under the inverse scattering transform. We also estimated the energy, skewness and asymmetry as functions of time and pressure magnitude. For onshore wind (positive P), wave energy and skewness increased with time while asymmetry decreased, while offshore wind produced the opposite effects. Furthermore, these effects were enhanced for strong pressures, and they reduced to the unforced case for $P = 0$. The shape statistics found here show qualitative agreement with the results in intermediate and deep water. Finally, the wind speeds corresponding to these pressure differences were calculated and found to be physically realistic.

We are grateful to D. G. Grimes and M. S. Spydell for discussions on this work. We thank the National Science Foundation (OCE-1558695) and the Mark Walk Wolfinger Surfzone Processes Research Fund for their support of this work. Declaration of Interests. The authors report no conflict of interest.

REFERENCES

- ANTAR, N. & DEMIRAY, H. 1999 Weakly nonlinear waves in a prestressed thin elastic tube containing a viscous fluid. *International journal of engineering science* **37** (14), 1859–1876.
- BANNER, M. L. & MELVILLE, W. K. 1976 On the separation of air flow over water waves. *Journal of Fluid Mechanics* **77** (04), 825–842.
- DONELAN, M. A., BABANIN, A. V., YOUNG, I. R. & BANNER, M. L. 2006 Wave-follower field measurements of the wind-input spectral function. part ii: Parameterization of the wind input. *Journal of Physical Oceanography* **36** (8), 1672–1689.
- DRAKE, T. G. & CALANTONI, J. 2001 Discrete particle model for sheet flow sediment transport in the nearshore. *Journal of Geophysical Research: Oceans* **106** (C9), 19859–19868.
- FEDDERSEN, F. & VERON, F. 2005 Wind effects on shoaling wave shape. *Journal of Physical Oceanography* **35** (7), 1223–1228.
- HAMMACK, J. L. & SEGUR, H. 1974 The Korteweg-de Vries equation and water waves. part 2. comparison with experiments. *Journal of Fluid mechanics* **65** (2), 289–314.
- HAYNE, G. 1980 Radar altimeter mean return waveforms from near-normal-incidence ocean surface scattering. *IEEE Transactions on Antennas and Propagation* **28** (5), 687–692.
- HOEFEL, F. & ELGAR, S. 2003 Wave-induced sediment transport and sandbar migration. *Science* **299** (5614), 1885–1887.
- HUSAIN, N. T., HARA, T., BUCKLEY, M. P., YOUSEFI, K., VERON, F. & SULLIVAN, P. P. 2019 Boundary layer turbulence over surface waves in a strongly forced condition: LES and observation. *Journal of Physical Oceanography* **49** (8), 1997–2015.
- JANSSEN, P. A. E. M. 1991 Quasi-linear theory of wind-wave generation applied to wave forecasting. *Journal of Physical Oceanography* **21** (11), 1631–1642.
- JEFFREYS, H. 1925 On the formation of water waves by wind. *Proc. R. Soc. Lond. A* **107** (742), 189–206.
- KIVSHAR, Y. S. 1993 Dark solitons in nonlinear optics. *IEEE Journal of Quantum Electronics* **29** (1), 250–264.
- LEYKIN, I. A., DONELAN, M. A., MELLEN, R. H. & MCLAUGHLIN, D. J. 1995 Asymmetry of wind waves studied in a laboratory tank. *Nonlinear Processes in Geophysics* **2** (3/4), 280–289.
- MEI, C. C., STIASSNIE, M. & YUE, D. K. P. 2005 *Theory and Applications of Ocean Surface Waves: Nonlinear Aspects*. *Advanced Series on Ocean Engineering* 2. World Scientific.
- MILES, J. W. 1957 On the generation of surface waves by shear flows. *Journal of Fluid Mechanics* **3** (2), 185–204.
- PHILLIPS, O. M. 1957 On the generation of waves by turbulent wind. *Journal of Fluid Mechanics* **2** (5), 417–445.
- SAHU, B. & TRIBECHÉ, M. 2012 Nonextensive dust acoustic solitary and shock waves in nonplanar geometry. *Astrophysics and Space Science* **338** (2), 259–264.
- SANDSTROM, H. & OAKEY, N. 1995 Dissipation in internal tides and solitary waves. *Journal of Physical Oceanography* **25** (4), 604–614.
- SOARES, G. C., FONSECA, N. & PASCOAL, R. 2008 Abnormal wave-induced load effects in ship structures. *Journal of ship research* **52** (1), 30–44.
- SULLIVAN, P. P. & MCWILLIAMS, J. C. 2010 Dynamics of winds and currents coupled to surface waves. *Annual Review of Fluid Mechanics* **42** (1), 19–42.
- TIAN, Z. & CHOI, W. 2013 Evolution of deep-water waves under wind forcing and wave breaking effects: Numerical simulations and experimental assessment. *European Journal of Mechanics-B/Fluids* **41**, 11–22.
- TOUBOUL, J. & KHARIF, C. 2006 On the interaction of wind and extreme gravity waves due to modulational instability. *Physics of Fluids* **18** (10), 108103.
- ZDYRSKI, T. & FEDDERSEN, F. 2020 Wind-induced changes to surface gravity wave shape in deep to intermediate water. *Journal of Fluid Mechanics* In press.
- ZDYRSKI, T. & MCGREEVY, J. 2019 Effects of dissipation on solitons in the hydrodynamic regime of graphene. *Physical Review B* **99** (23), 235435.